separations

MDPI

Article

Porous Spherical Granulation of Co-Doped Manganese-Based Lithium Ion-Sieve with Solid Paraffin as Mesoporous Porogen for Lithium Recovery from Salt Lake Brine

Qiansheng Liu, Zhiqiang Hu, Ming Li and Xichang Shi *

School of Metallurgy and Environment, Central South University, Changsha 410083, China; 253512082@csu.edu.cn (Q.L.); 233512143@csu.edu.cn (Z.H.); 243512184@csu.edu.cn (M.L.)
* Correspondence: xichangshi@csu.edu.cn

Abstract

Manganese-based lithium ion-sieves (LIS) are promising adsorbents for lithium extraction from salt lake brines. Their powder form, however, hinders industrial application because it disperses poorly, is difficult to recover, and causes excessive pressure drop in fixed-bed columns. Here we address this powder-forming challenge through porous spherical granulation, using solid paraffin as a mesoporous porogen. Co-doped precursors were prepared by hydrothermal calcination. XPS showed that Co doping raised the Mn^{4+} ratio from 65.77% to 72.16%, which suppresses the Jahn-Teller effect. The optimal powder reached 33.36 mg/g in LiCl solution and retained 89.0% of this capacity after five cycles. For granulation, the powder was modified with octadecyltrimethoxysilane (OTMS) and granulated by suspension polymerization. The solid paraffin porogen created mesoporous channels that increased the BET surface area from 0.82 to 82.00 m^2/g. The optimized granule reached 4.42 mg/g in LiCl solution and 1.56 mg/g in real salt lake brine, with separation factors of 357.0, 256.5, 225.4, and 41.87 for Na^+, K^+, Mg^{2+}, and Ca^{2+}, respectively. It kept 62% of its capacity after 20 cycles, and Mn dissolution stabilized at 0.18%. The combined doping and pore-engineering strategy offers a viable route to lithium extraction from salt lake brines.

Keywords: lithium ion-sieve; Co doping; suspension granulation; solid paraffin; mesoporous porogen; salt lake brine

1. Introduction

Lithium is a key metal for the new energy industry, used in lithium-ion batteries, energy storage systems, and other high-technology applications [1–4]. Salt lake brines hold more than half of the world's lithium reserves and have become the main source of supply because they are abundant and cheap to extract [5]. Yet separating Li^+ from these brines is difficult: coexisting ions (Na^+, K^+, Ca^{2+}, Mg^{2+}) are present at concentrations orders of magnitude higher than that of Li^+ [6–8]. Several separation technologies have been explored, including membrane-based separation [9] and adsorption by lithium ion-sieves (LIS), the latter studied widely for its high selectivity and low energy consumption [10,11].

Spinel-type manganese-based LIS have been studied as adsorbents for Li^+ separation since λ-MnO_2 was first prepared by acid leaching of $LiMn_2O_4$ [12–16]. These spinel structures contain a three-dimensional diffusion channel for Li^+, and adsorption–desorption proceeds by the reversible insertion and extraction of Li^+ [17]. Two problems, however,

Check for updates

Academic Editors: Sen Lin, Jun Chen and Hao Jiang

Received: 7 September 2026
Revised: 23 September 2026
Accepted: 29 September 2026
Published: 30 September 2026

Copyright: © 2026 by the authors. Licensee MDPI, Basel, Switzerland. This article is an open access article distributed under the terms and conditions of the Creative Commons Attribution (CC BY) license.

impede large-scale application. First, Mn^{3+} in the spinel induces the Jahn-Teller effect and disproportionation reactions, causing severe manganese dissolution during cycling and, in turn, structural degradation and capacity decay [18]. Second, the powder form disperses poorly in brine, is difficult to recover, and creates excessive pressure drop in fixed-bed columns, so it is unsuitable for continuous industrial operations [19].

Element doping, particularly Co substitution, suppresses Mn dissolution by raising the Mn^{4+} ratio and easing the Jahn-Teller distortion [20–22]. Doping solves the stability problem, but the powder-forming problem needs a different approach. Several granulation strategies have been tried, including polyvinyl chloride/polyacrylonitrile (PVC/PAN) composite granulation [23], sodium alginate composite granules [24], half-coated manganese oxide LIS [25], spherical manganese-based LIS [26], β–cyclodextrin/polyvinylidene fluoride (PVDF) composite membranes [27], and hollow hemispherical mixed matrix adsorbents [28–31]. Suspension polymerization of polymerizable monomers is attractive because the particle size is controllable and the mechanical strength is good [32,33]. One limitation persists, however: the polymer matrix encapsulates part of the active adsorbent and blocks Li^+–containing solution from the interior adsorption sites. This causes a large loss of adsorption capacity that existing porogen strategies have not resolved [34–36].

Conventional porogens such as toluene mainly generate micropores, which cannot let viscous brine penetrate deeply into the particle interior [37]. Some loss of adsorption capacity after granulation is an inherent, recognized trade-off in polymer-encapsulated adsorbent systems [38]: the inert polymer matrix dilutes the active component and blocks some adsorption sites. Granulation is valuable not for matching powder-level capacity but for solving the engineering problems of powder dispersibility, column blockage, and adsorbent loss during continuous operation. These problems make powder adsorbents impractical for industrial use even when their intrinsic capacity is high [39].

In this study, we address the powder-forming challenge through a pore-engineering approach to suspension granulation. A Co-doped lithium ion-sieve powder was first synthesized to ensure structural stability. Solid paraffin was then used as the mesoporous porogen during suspension polymerization. Unlike liquid porogens such as toluene, which generate only micropores, solid paraffin is molten at the polymerization temperature and acts as a non-solvating porogen. It separates into discrete domains through polymerization-induced phase separation and, once removed by Soxhlet extraction, leaves mesoporous channels. This approach raises the specific surface area from 0.82 to 82.00 m^2/g, while adsorption capacity improves by 75% (from 2.52 to 4.42 mg/g) because the polymer matrix still makes up about 80 wt% of the particle. The larger surface area turns the granule from a largely inaccessible composite into a porous sphere with accessible active sites. This is the first report of solid paraffin as a mesoporous porogen for LIS granulation, providing interconnected mesoporosity that conventional micropore-forming porogens cannot.

2. Materials and Methods

2.1. Materials

Lithium hydroxide monohydrate ($LiOH{\cdot}H_2O$, analytical grade, Innochem, Beijing, China), manganese(III) oxide (Mn_2O_3, laboratory-prepared), cobalt(II) chloride hexahydrate ($CoCl_2{\cdot}6H_2O$, analytical grade, Haohong Biological, Shanghai, China), styrene (C_8H_8, analytical grade, Sinopharm, Shanghai, China), divinylbenzene ($C_{10}H_{10}$, analytical grade, Macklin, Shanghai, China), benzoyl peroxide ($C_{14}H_{10}O_4$, ≥98%, Macklin, Shanghai, China), gelatin (analytical grade, Sinopharm, Shanghai, China), polyvinyl alcohol (analytical grade, Sinopharm, Shanghai, China), solid paraffin (chemical grade, Xi'an Jinxiang Pharmaceutical Excipients Co., Ltd., Xi'an, China), toluene (analytical grade, Hengxing Chemical, Tianjin, China), octadecyltrimethoxysilane (OTMS, Macklin, Shanghai, China), sodium do-

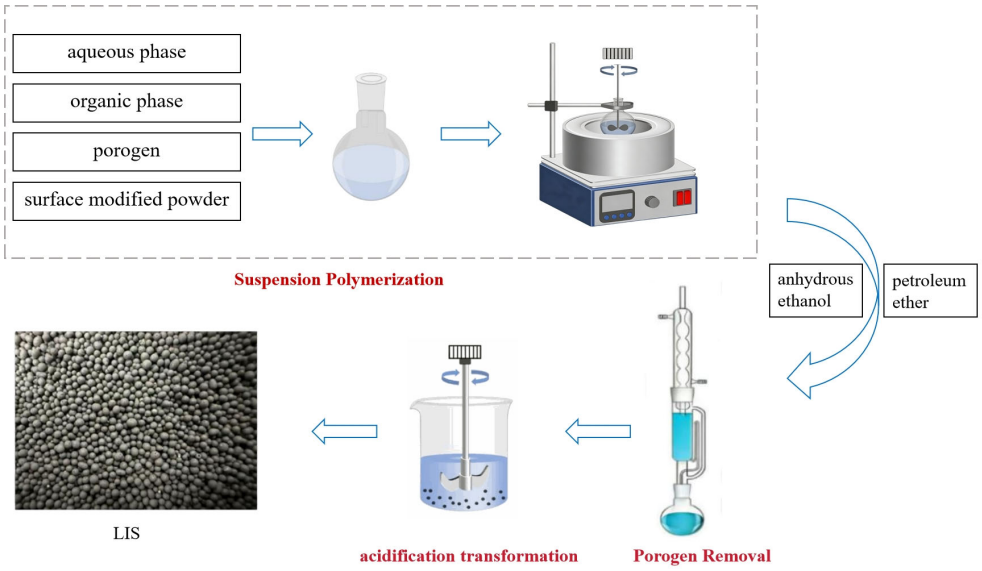
decylbenzenesulfonate (analytical grade, Sinopharm, Shanghai, China), anhydrous ethanol (analytical grade, Hengxing Chemical, Tianjin, China), petroleum ether (spectroscopic grade, Baishun Biological, Shanghai, China), hydrochloric acid (HCl, 36–38%, Kelong Chemical, Chengdu, China), and sodium hydroxide (NaOH, analytical grade, Macklin, Shanghai, China) were used. All solutions were prepared with deionized water.

2.2. Synthesis of Co-Doped Precursors

Co-doped $Li_{1.6}Mn_{1.6-x}Co_xO_4$ (x = 0, 0.02, 0.04, 0.06, 0.08) precursors were prepared via a two-step hydrothermal-calcination method. $LiOH{\cdot}H_2O$ and Mn_2O_3 were mixed at a Li/Mn molar ratio of 4:1. $CoCl_2{\cdot}6H_2O$ was added stoichiometrically according to the target x values. The mixture was transferred into a high-pressure autoclave and reacted at 200–230 °C for 15 h. The resulting $LiMnO_2$ intermediate was filtered, washed, dried, and calcined at 410 °C for 6 h to yield the precursors designated LMO, LMCO-2, LMCO-4, LMCO-6, and LMCO-8. These precursors were acid-treated in 200 mL of 0.5 mol/L HCl for 8 h to obtain the proton-exchanged ion-sieves HMO, HMCO-2, HMCO-4, HMCO-6, and HMCO-8. The Li transformation rate is defined as the molar percentage of Li extracted from the precursor during acid treatment relative to its total Li content.

2.3. Surface Modification and Suspension Granulation

The Co-doped powder was hydrophobically modified with OTMS. A 100 mL aqueous solution of sodium dodecylbenzenesulfonate (0.2 g/L) was mixed with OTMS and the Co-doped powder. The mixture was stirred at 65 °C for 2 h, filtered, dried at 120 °C for 4 h, and washed with anhydrous ethanol. The modified powder was then granulated via suspension polymerization using styrene and divinylbenzene as the polymer matrix, gelatin and polyvinyl alcohol as dispersants, and benzoyl peroxide as the initiator. The polymerization was conducted at 75 °C with stirring at 300 rpm for 4 h. Three granulated samples were prepared: (i) without porogen (Z-LMCO-4); (ii) with 30 wt% toluene relative to styrene (J-LMCO-4); and (iii) with 30 wt% solid paraffin relative to styrene (T-LMCO-4). Porogens were removed from samples (ii) and (iii) by Soxhlet extraction with petroleum ether. Subsequent acid treatment in 200 mL of 0.5 mol/L HCl for 24 h produced Z-HMCO-4, J-HMCO-4, and T-HMCO-4. The overall synthesis route is illustrated in Scheme 1.



Scheme 1. Synthesis route of porous spherical granulated lithium ion-sieve.

2.4. Characterization

Crystal phases were identified by X-ray diffraction (XRD, Rigaku TTRIII, Cu Kα radiation, Tokyo, Japan). Surface chemical states were analyzed by X-ray photoelectron spectroscopy (XPS, Thermo Fisher Scientific ESCALAB 250Xi, Waltham, MA, USA). Morphology was examined by scanning electron microscopy (SEM, JEOL JSM-7900F, Tokyo, Japan). Elemental distribution was analyzed by energy-dispersive X-ray spectroscopy (EDS, EDAX, Mahwah, NJ, USA) equipped on the SEM. Functional groups were characterized by Fourier-transform infrared spectroscopy (FT-IR, Thermo Fisher Scientific Nicolet iS50, Waltham, MA, USA). Surface wettability was measured by contact angle goniometry (Dataphysics OCA20, Filderstadt, Germany). Specific surface area and pore structure were determined by nitrogen adsorption–desorption (BET, Micromeritics ASAP2020HD88, Norcross, GA, USA). Prior to BET measurement, samples were outgassed at 85 °C for 12 h under vacuum. The mechanical strength of granulated samples was tested on a particle strength tester (YHKC-2A, Yinhe Instrument, Taizhou, China). Elemental concentrations in solution were quantified by inductively coupled plasma optical emission spectrometry (ICP-OES, Thermo Fisher Scientific ICAP7400, Waltham, MA, USA).

2.5. Adsorption Experiments

All adsorption experiments were performed in duplicate. The adsorption capacity at time t was calculated using Equation (1). For powder samples, 1 g of adsorbent was added to 200 mL of LiCl solution. For granulated samples, 3.5 g was added to 200 mL of solution (initial Li^+ concentration: 300 mg/L; pH = 10). Adsorption kinetics were studied at initial Li^+ concentrations of 100–500 mg/L and fitted to the pseudo-first-order (Equation (2)) and pseudo-second-order (Equation (3)) models [40,41]. The rate-controlling step was evaluated using the Weber-Morris intra-particle diffusion model (Equation (4)) [41]. Adsorption isotherms were measured at 303, 318, and 333 K and fitted to the Langmuir (Equation (5)) and Freundlich (Equation (6)) models [42,43]. The solution pH was adjusted and maintained at 10 using a buffer solution. Selectivity and cycling stability were evaluated using actual salt lake brine from Xinjiang, China. Powder selectivity tests were conducted by dispersing the adsorbent in 200 mL of brine at room temperature for 24 h.

The pH dependence of powder adsorption was evaluated in lithium-containing buffer solutions at pH 6, 8, 10, and 12 (initial Li^+ concentration 300 mg/L, contact time 24 h); the results are discussed in Section 3.5.

Granule selectivity and cycling tests were performed in a fixed-bed glass column (inner diameter 15 mm, bed height 120 mm, bed volume ≈ 21 mL, bed charge ≈ 6.3 g) packed with T-HMCO-4 granules, with filter nets at both ends to retain the granules and to remove suspended solids from the brine. In each run, 200 mL of brine (Li^+ 125 mg/L, Na^+ 27.7 g/L, K^+ 23.9 g/L, Mg^{2+} 63.1 g/L, Ca^{2+} 31.7 mg/L, pH 5.30) from Xinjiang, China, was circulated through the bed in a closed loop at 20 mL/min with a peristaltic pump until the bed reached saturation after about 24 h. Samples of the circulating brine were taken periodically and analyzed by ICP-OES. After saturation, the bed was washed with deionized water, eluted with 200 mL of 0.5 mol/L HCl, and washed again with deionized water before the next adsorption cycle.

$$Q_t = \frac{(C_0 - C_t) \times V}{m} \quad (1)$$

where C_0 and C_t (mg/L) are the initial and time-t Li^+ concentrations, V (L) is the solution volume, and m (g) is the adsorbent mass.

$$\ln(Q_e - Q_t) = \ln Q_e - K_1 \times t \quad (2)$$

where Q_e and Q_t (mg/g) are the equilibrium and time-t adsorption capacities, and K_1 (h^{-1}) is the pseudo-first-order rate constant.

$$\frac{t}{Q_t} = \frac{1}{K_2 \times {Q_e}^2} + \frac{t}{Q_e} \quad (3)$$

where K_2 (g/(mg·h)) is the pseudo-second-order rate constant, and Q_e (mg/g) is the equilibrium adsorption capacity.

$$Q_t = K_d \times t^{0.5} + C \quad (4)$$

where K_d (mg/(g·$h^{0.5}$)) is the intra-particle diffusion rate constant, and C is a constant related to the boundary layer thickness.

$$\frac{C_e}{Q_e} = \frac{C_e}{Q_m} + \frac{1}{Q_m \times K_L} \quad (5)$$

where Q_m (mg/g) is the maximum adsorption capacity, K_L (L/mg) is the Langmuir constant, and C_e (mg/L) is the equilibrium concentration.

$$\ln Q_e = \ln K_F + \frac{1}{n} \times \ln C_e \quad (6)$$

where K_F and n are the Freundlich constants related to adsorption capacity and intensity, respectively.

$$\Delta G^\theta = -R \times T \times \ln K_d^\theta \quad (7)$$

where ΔG^θ (kJ/mol) is the standard Gibbs free energy change, R (8.314 J/(mol·K)) is the gas constant, T (K) is the temperature, and K_d^θ is the dimensionless equilibrium constant (distribution coefficient).

$$\ln K_d^\theta = \frac{\Delta S}{R} - \frac{\Delta H}{R \times T} \quad (8)$$

where ΔS (J/(mol·K)) is the entropy change and ΔH (kJ/mol) is the enthalpy change.

$$\alpha\left(Li^+/M_i\right) = \frac{K_{Li}}{K_i} \quad (9)$$

where K_i (L/g) is the distribution coefficient of ion i, calculated as $K_i = (C_{0,i} - C_{e,i}) \times V/(m \times C_{e,i})$, and α (Li^+/M_i) is the separation factor defined as the ratio of K_{Li} to K_i.

3. Results and Discussion

3.1. Structural Characterization of Co-Doped Ion-Sieve

XRD patterns (Figure 1a) showed that all Co-doped precursors matched the standard spinel structure (JCPDS 52-1841, $Fd^{-3}m$), with no Co-related impurity peaks. This indicates that Co^{3+} substituted Mn^{3+} in the spinel lattice. After acid treatment, HMCO-4 kept the spinel structure, with diffraction peaks shifting to higher angles (Figure 1b), consistent with lattice contraction from Li^+ replacement by the smaller H^+.

SEM images (Figure 2) showed octahedral morphologies (100–200 nm) for both LMCO-4 and HMCO-4, with no change after acid treatment. EDS mapping confirmed that Mn, Co, and O were distributed uniformly.

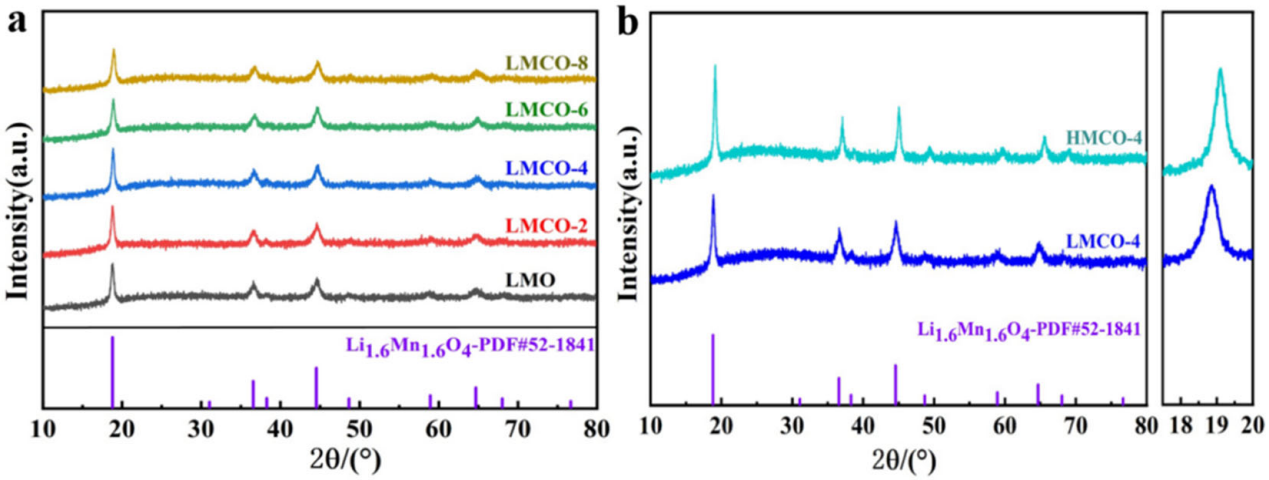


Figure 1. XRD patterns: (**a**) Co-doped precursors (LMO, LMCO-2, LMCO-4, LMCO-6, LMCO-8); (**b**) LMCO-4 and HMCO-4 after acid treatment.

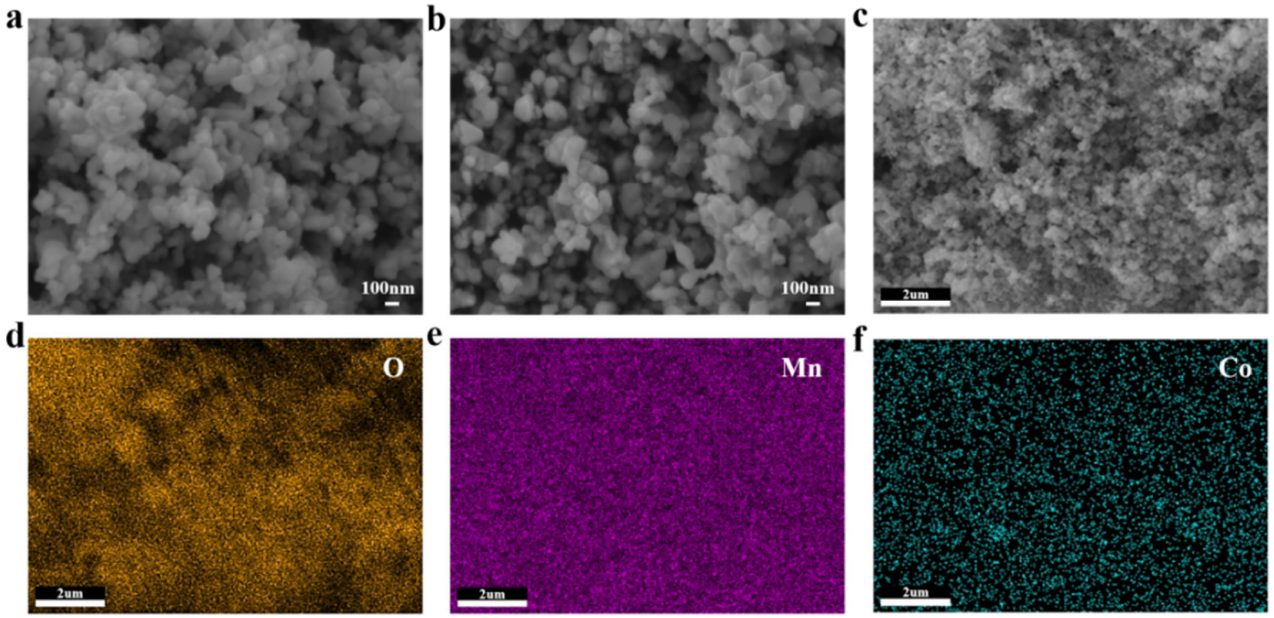


Figure 2. SEM images of (**a**) LMCO-4 and (**b**) HMCO-4; (**c**–**f**) EDS elemental mapping of LMCO-4.

XPS analysis (Figure 3) revealed the doping mechanism. The survey scan of LMCO-4 showed characteristic peaks of Mn_2p, O1s, C_1s, and Co2p, and the $Co2p_{3/2}$ peak at 780.5 eV confirmed that the doped Co is trivalent (Co^{3+}). Deconvolution of $Mn2p_{3/2}$ gave Mn^{4+} (642.88 eV) and Mn^{3+} (641.96 eV). Co substitution raised the Mn^{4+} ratio from 65.77% to 72.16% and lowered Mn^{3+} from 34.23% to 27.84%. This drop in Mn^{3+} matters because Mn^{3+} is the main trigger of the Jahn-Teller distortion and of the disproportionation reaction ($2Mn^{3+} \rightarrow Mn^{4+} + Mn^{2+}$) that causes manganese dissolution [44]. O_1s analysis indicated that Co doping promoted the formation of lattice oxygen [MnO_6]. The binding energy of lattice oxygen in LMCO-4 (529.5 eV) was close to that in undoped LMO (529.56 eV), consistent with the spinel framework staying intact after Co substitution.

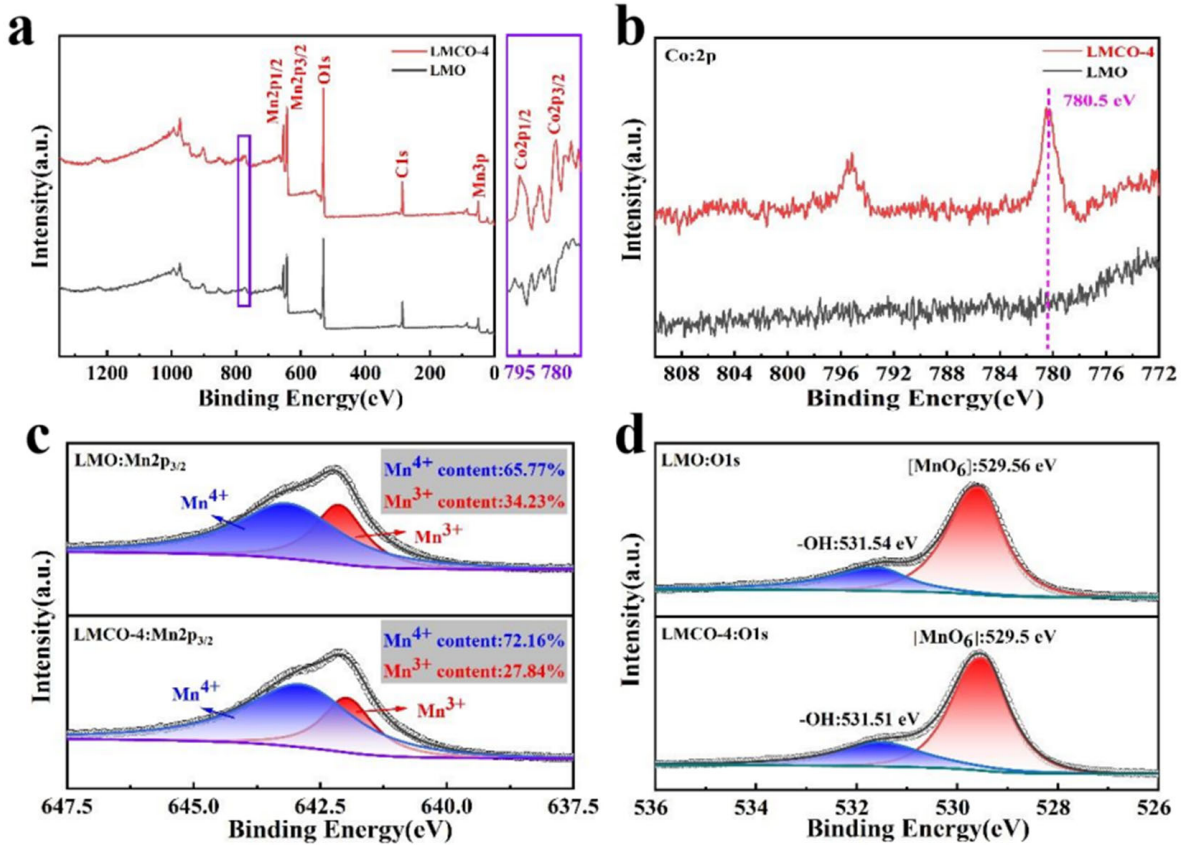


Figure 3. XPS spectra of LMCO-4: (**a**) survey scan; (**b**) Co2p; (**c**) Mn2p; (**d**) O1s.

3.2. Adsorption Performance, Selectivity, and Cycling Stability of Co-Doped Powder

Figure 4a shows the effect of Co doping on acid treatment efficiency. The Li transformation rate peaked at 89.67% for LMCO-4, while Mn dissolution was lowest at 2.65%. Adsorption capacities (Figure 4b) followed the order HMO (31.26) < HMCO-2 (32.45) < HMCO-4 (33.36) > HMCO-6 (31.53) > HMCO-8 (30.11) mg/g, consistent with x = 0.04 as the optimal doping level.

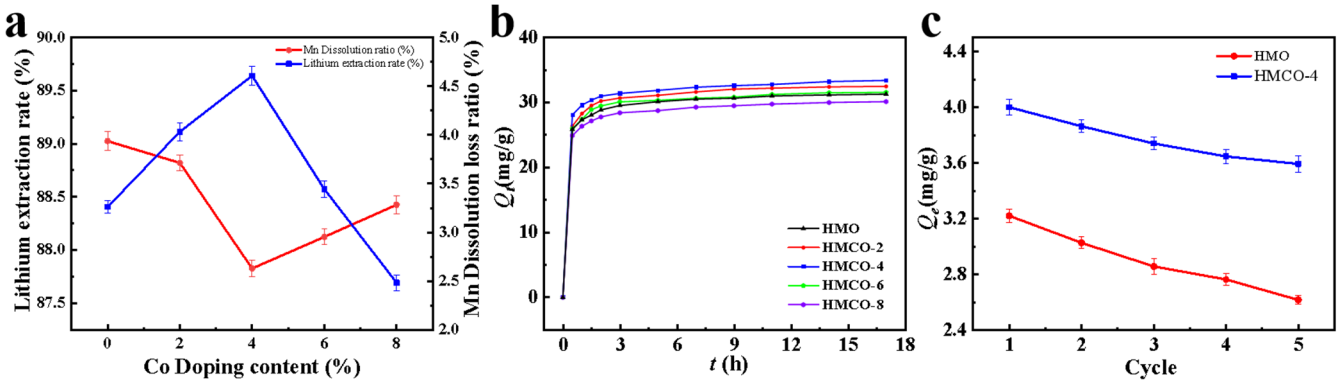


Figure 4. (**a**) Effect of Co doping level on acid treatment; (**b**) Adsorption capacities of Co-doped powder ion-sieves at different Co doping levels; (**c**) Cycling performance of HMO and HMCO-4 over 5 adsorption–desorption cycles.

After five adsorption–desorption cycles, HMCO-4 retained 89.0% of its initial capacity, better than undoped HMO (80.8%) (Figure 4c). This improvement reflects the lower Mn dissolution from Co doping.

Beyond capacity and cycling stability, the powder HMCO-4 showed high selectivity for Li^+ over coexisting ions in real salt lake brine. This selectivity comes from the three-dimensional diffusion channels of the spinel structure [45]. Ions larger than Li^+ (0.074 nm), such as Na^+ (0.102 nm), K^+ (0.138 nm), and Ca^{2+} (0.1 nm), are excluded by steric hindrance. Mg^{2+} (0.072 nm) has a radius close to Li^+, but its hydration free energy (1830 kJ/mol) is far higher than that of Li^+ (475 kJ/mol) [46], so it is also hindered. In actual salt lake brine, HMCO-4 reached 22.79 mg/g, with separation factors of 257.71, 142.42, 676.50, and 5.15 for Na^+, K^+, Mg^{2+}, and Ca^{2+}, respectively (Table 1).

Table 1. Adsorption selectivity of HMCO-4 powder in actual salt lake brine.

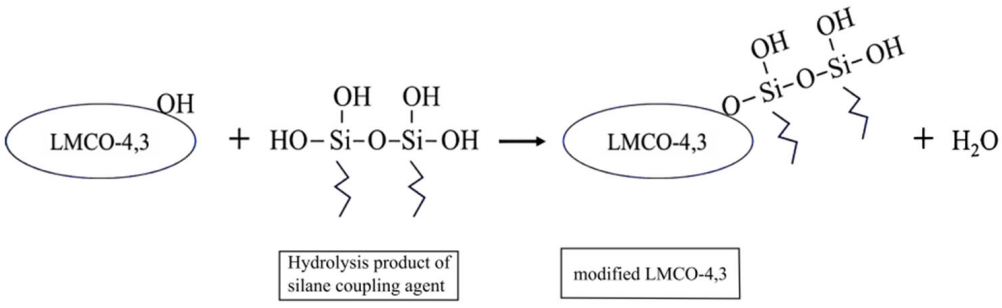
Ions	C_0 (mg/L)	$C_{e,i}$ (mg/L)	K_i (L/g)	α (Li^+/M_i)
Li^+	128.8	42.1	0.5412	1
Na^+	32,070	31,820	0.0021	257.71
K^+	22,220	21,900	0.0038	142.42
Mg^{2+}	70,360	70,140	0.0008	676.50
Ca^{2+}	52.55	37.55	0.105	5.15

3.3. Surface Modification and Granulation with Solid Paraffin Porogen

Before granulation, the Co-doped powder was made hydrophobic with OTMS so that it would mix with the organic monomer phase. In this modification, OTMS hydrolyzes to silanol groups (-Si-OH), which bond chemically with the hydroxyl groups (-OH) on the powder and graft hydrophobic long-chain alkyl groups onto the surface [47] (Scheme 2). FT-IR (Figure 5) confirmed the grafting: characteristic peaks appeared at 1091.4 cm^{-1} (Si-O-Si asymmetric stretching) and 2852.2/2925.9 cm^{-1} (-CH_2- symmetric and asymmetric stretching). The contact angle rose from 23.09° to 149.62° (Figure 6), changing the surface from hydrophilic to hydrophobic so the powder dispersed uniformly in the organic monomer phase during suspension granulation.

Three granulated adsorbents were prepared: Z-LMCO-4 (no porogen), J-LMCO-4 (toluene porogen), and T-LMCO-4 (solid paraffin porogen). SEM images (Figure 7) showed that all particles were spherical but had different internal structures. Z-LMCO-4 was dense with few pores, J-LMCO-4 had limited porosity, and T-LMCO-4 showed the most abundant mesopores throughout the particle.

The BET surface areas of Z-LMCO-4, J-LMCO-4, and T-LMCO-4 were 0.82, 8.83, and 82.00 m^2/g, respectively (Table 2). BET was measured before acid treatment to isolate the porogen effect from acid-induced structural changes. N_2 adsorption–desorption of T-LMCO-4 (Figure 8) gave a Type IV isotherm with a distinct hysteresis loop at P/P_0 = 0.5–1.0, consistent with a mesoporous material.



Scheme 2. Reaction mechanism of OTMS surface modification of the Co-doped powder.

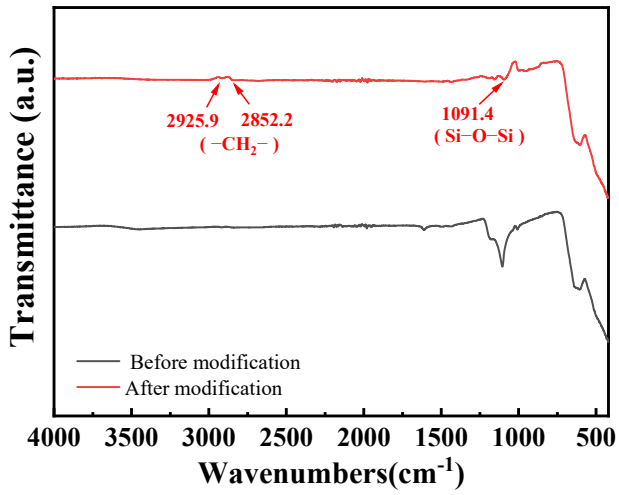


Figure 5. FT-IR spectra of the Co-doped powder before and after OTMS surface modification.

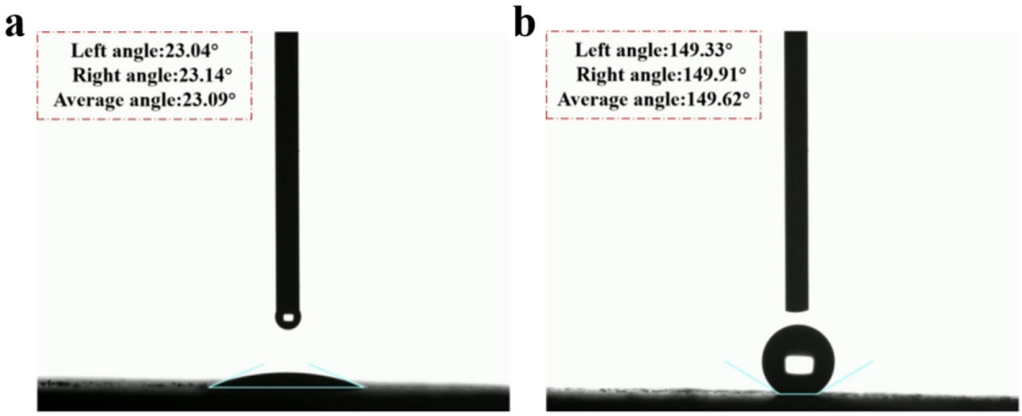


Figure 6. Contact angle measurements: (**a**) before OTMS modification (23.09°); (**b**) after modification (149.62°).

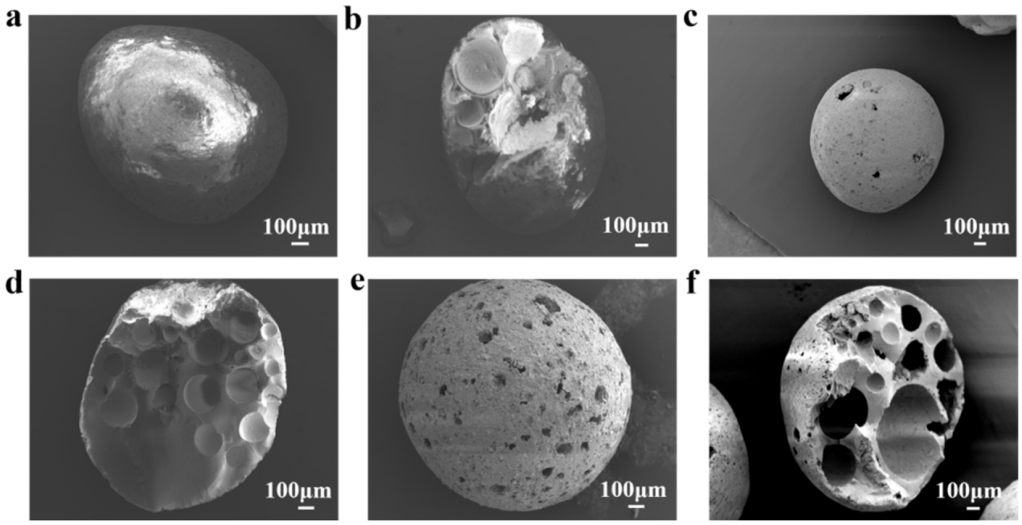


Figure 7. SEM images of (**a**,**b**) no porogen; (**c**,**d**) toluene porogen; (**e**,**f**) solid paraffin porogen.

Table 2. BET surface area, pore structure parameters, and mechanical strength of the granulated samples.

Property	Z-LMCO-4	J-LMCO-4	T-LMCO-4
BET (m^2/g)	0.82	8.83	82.00
Pore diam. (nm)	-	-	8.248
Strength (N)	8.42	8.18	6.39
Active comp. (%)	20.71	20.44	20.57
Li transf. (%)	8.35	10.67	14.83
Mn dissol. (%)	0.75	0.96	1.25

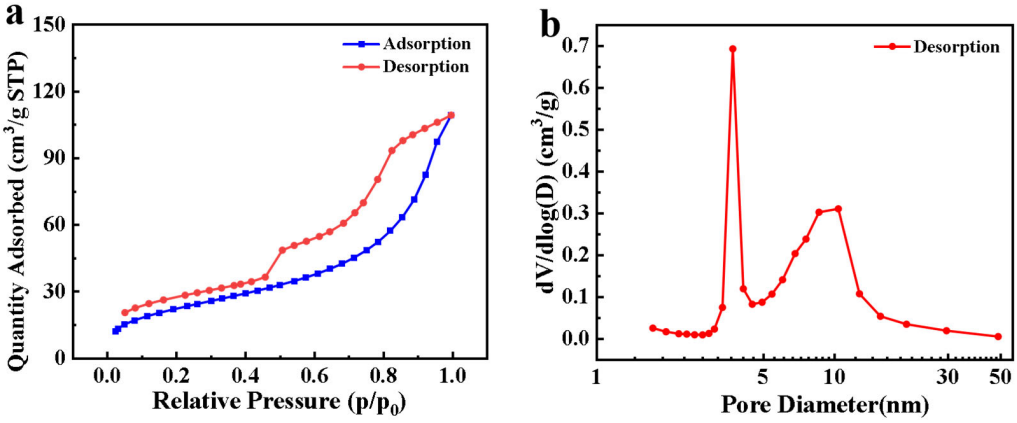


Figure 8. N_2 adsorption–desorption analysis of T-LMCO-4: (**a**) isotherm curve; (**b**) pore size distribution.

Solid paraffin differs from conventional porogens. Toluene is miscible with the monomer phase and mainly generates micropores, which are insufficient for brine penetration. Solid paraffin is molten at the polymerization temperature (75 °C) and acts as a non-solvating porogen. It separates into discrete domains through polymerization-induced phase separation and, once removed by Soxhlet extraction, leaves mesoporous channels (average pore diameter 8.248 nm, pore volume 0.169 cm^3/g). These mesopores form continuous paths from the particle surface to its core, letting the lithium-containing solution reach interior active components that would otherwise stay encapsulated.

The three samples had similar active component contents (20.71%, 20.44%, and 20.57% for Z-LMCO-4, J-LMCO-4, and T-LMCO-4), which indicates that the porogen does not react with the adsorbent but acts as a physical template. Acid treatment efficiency differed: Li transformation rates were 8.35%, 10.67%, and 14.83%, reflecting limited acid access through the polymer matrix. This low transformation rate contributes strongly to the reduced capacity, because unextracted Li^+ occupies sites that would otherwise be available for re-adsorption. Longer acid treatment or higher acid concentrations may raise the transformation rate, although excessive acid could damage the structure. Mn dissolution stayed below 1.25% in all samples, so granulation preserves structural integrity during acid treatment.

Several routes are available to improve acid penetration without compromising the spinel framework. The present comparison already identifies the dominant factor: at identical acid conditions (0.5 mol/L HCl), replacing the porogen-free formulation with solid paraffin raised the Li transformation rate from 8.35% to 14.83%, because the interconnected mesopores shorten the diffusion path of the acid into the particle interior. Further gains can be expected from (i) a higher porogen-to-monomer ratio, which would further open and interconnect the pore network; (ii) a smaller granule diameter, which shortens the internal diffusion length; (iii) a higher acid concentration or temperature, which accelerates H^+/Li^+ exchange but must be balanced against accelerated Mn dissolution; and (iv) a more

hydrophilic binder chemistry, for example, post-granulation sulfonation of the St/DVB network or copolymerization with hydrophilic monomers.

Mechanical strength fell from 8.42 N (Z) to 6.39 N (T) because of pore formation, yet stayed within the range acceptable for column packing.

The ≈80 wt% polymer fraction is dictated by the requirements of suspension granulation. The OTMS-modified powder must remain fully dispersed in the organic monomer phase; higher powder loadings raise the slurry viscosity and cause agglomeration, yielding deformed or irregular granules. In addition, pore formation already lowers the mechanical strength from 8.42 N (Z-LMCO-4) to 6.39 N (T-LMCO-4), and a further reduction in the polymer fraction would push the strength below what fixed-bed packing requires. Reducing the polymer content to 40–50 wt% therefore requires a simultaneous reformulation: (i) a dispersion route for higher powder loadings (for example, finer OTMS-modified powder or surfactant-assisted suspension); (ii) a more highly crosslinked or filler-reinforced matrix to maintain strength; and (iii) re-optimized porogen levels, since less polymer leaves less pore wall to maintain the sphere. The incentive for such a reformulation is quantified by the capacity data of Section 3.4: at the current active loading of about 20.6 wt%, the granule delivers ≈ 21.5 mg of Li per gram of LIS, i.e., 64% of the powder value. Provided that site utilization is maintained, the granule capacity scales nearly proportionally with the active fraction. We also note that the process economics are governed by the cumulative Li^+ throughput over the service life rather than by the single-cycle capacity: with 62% capacity retention after 20 cycles and Mn dissolution stabilized at 0.18%, the granule remains productive over many more cycles than were tested here.

3.4. Adsorption Kinetics and Thermodynamics of Granulated Adsorbent

The adsorption capacities of the three granules followed the same order as their BET areas: T-HMCO-4 (4.42 mg/g) > J-HMCO-4 (3.24 mg/g) > Z-HMCO-4 (2.52 mg/g) (Figure 9a). This direct correlation shows that the mesoporous structure created by solid paraffin allows access to the interior adsorption sites.

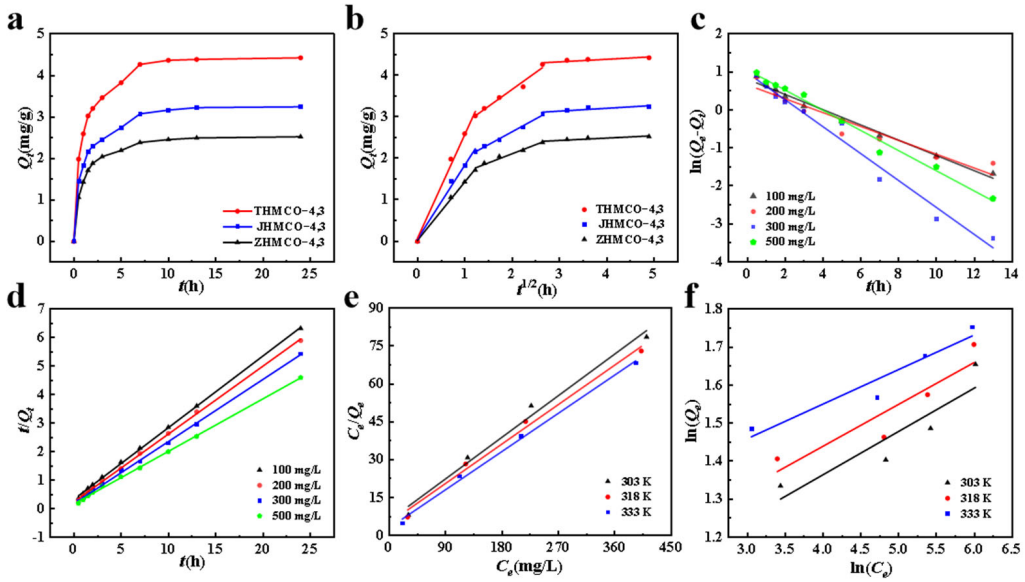


Figure 9. (**a**) Adsorption curves of three granulated ion-sieves; (**b**) Intra-particle diffusion model fitting for T-HMCO-4; (**c**,**d**) Pseudo-first-order and pseudo-second-order kinetic model fitting; (**e**,**f**) Langmuir and Freundlich isotherm models at different temperatures.

The capacity of the granule (4.42 mg/g) is lower than that of the powder (33.36 mg/g), and the loss can be decomposed into four sequential factors. First, dilution: the inert St/DVB matrix accounts for about 80 wt% of the granule, so even with fully accessible sites the granule capacity is capped at 33.36 mg/g × 0.206 ≈ 6.9 mg/g. Second, incomplete acid transformation: only 14.83% of the lattice Li^+ in the granule was converted to the H+ form (versus 89.67% for the free powder), and Li^+-occupied sites cannot participate in re-adsorption. Third, site sealing: a fraction of the active powder is fully encapsulated by the polymer and has no solution access. Fourth, the residual hydrophobic OTMS layer slows the wetting of internal pore surfaces. Normalized to the active LIS content (about 20.6 wt%), the granule delivers ≈ 21.5 mg of Li per gram of LIS, i.e., 64% of the powder value, which quantitatively reflects the second to fourth factors. The 75% capacity gain over the non-porogen control (from 2.52 to 4.42 mg/g) shows that solid-paraffin mesopores alleviate, but do not eliminate, these constraints.

Intra-particle diffusion analysis (Figure 9b) showed three adsorption stages: rapid external diffusion of Li^+ to the particle surface (K_{d1} = 2.498), slower intra-particle diffusion through the pores (K_{d2} = 0.817), and adsorption saturation (K_{d3} = 0.062) (Table 3). The C values were non-zero at all stages, so intra-particle diffusion is the main rate-limiting step but not the only one. Both Kd_1 and Kd_2 of T-HMCO-4 were higher than those of Z-HMCO-4 (1.405, 0.439) and J-HMCO-4 (1.775, 0.622), indicating that the mesoporous structure reduces both external and internal mass-transfer resistance. The pseudo-second-order model (R^2 = 0.999) fit better than the pseudo-first-order model (R^2 = 0.915–0.985) (Figure 9(c,d), Table 4), indicating that the H^+/Li^+ ion-exchange step is rate-limiting. The C values (C_1 = 0.067, C_2 = 2.020, C_3 = 4.133) indicate an increasing boundary-layer thickness at later stages.

Table 3. Intra-particle diffusion fitting parameters for the three granulated ion-sieves.

Sample	K_{d1}	C_1	R^2	K_{d2}	C_2	R^2	K_{d3}	C_3	R^2
Z-HMCO-4	1.405	0.020	0.997	0.439	1.228	0.965	0.057	2.256	0.734
J-HMCO-4	1.775	0.054	0.986	0.622	1.391	0.991	0.069	2.927	0.626
T-HMCO-4	2.498	0.067	0.989	0.817	2.020	0.967	0.062	4.133	0.659

Table 4. Kinetic fitting parameters for T-HMCO-4.

C_0 (mg/L)	Pseudo-First-Order			Pseudo-Second-Order			$Q_{e\text{-}exp}$ (mg/g)
	$Q_{el\text{-}cal}$ (mg/g)	K_1 (h^{-1})	R^2	$Q_{el\text{-}cal}$ (mg/g)	K_2 (g/(mg·h))	R^2	
100	2.24	0.200	0.985	3.98	0.193	0.999	3.80
200	1.92	0.182	0.915	4.20	0.241	0.999	4.07
300	2.65	0.354	0.972	4.59	0.276	0.999	4.42
500	2.85	0.265	0.985	5.43	0.202	0.999	5.23

Isotherm analysis (Figure 9e,f, Table 5) compared the Langmuir (Equation (5)) and Freundlich (Equation (6)) models. The Langmuir model (R^2 = 0.98–0.99; Q_m = 5.47, 5.76, and 5.95 mg/g; K_L = 0.031, 0.035, and 0.057 L/mg at 303, 318, and 333 K) described the adsorption better than the Freundlich model (R^2 = 0.75–0.88), consistent with monolayer adsorption on homogeneous sites [42,43]. The standard Gibbs free energy change ΔG^θ was obtained from Equation (7), and ΔH and ΔS were derived from the van't Hoff equation (Equation (8)) [48], where K_d^θ is the dimensionless equilibrium constant (distribution coefficient). The positive ΔH (16.86 kJ/mol) indicates an endothermic process, and the negative ΔG^θ (−13.53 to −16.56 kJ/mol) confirms spontaneous adsorption (Table 6). The positive ΔS (99.77 J/(mol·K)) suggests greater disorder at the solid–liquid interface during adsorption.

Adsorption capacity rose from 4.42 mg/g (303 K) to 5.35 mg/g (333 K), consistent with the endothermic nature.

Table 5. Langmuir and Freundlich isotherm fitting parameters for Li^+ adsorption on T-HMCO-4.

Sample	T (K)	Q_m (mg/g)	K_L (L/mg)	R^2	K_F (L/g)	n	R^2
T-HMCO-4	303	5.47	0.031	0.98	2.481	8.784	0.75
	318	5.76	0.035	0.99	2.714	9.079	0.78
	333	5.95	0.057	0.99	3.277	11.02	0.88

Table 6. Thermodynamic parameters for Li^+ adsorption on T-HMCO-4.

T (K)	K_d^θ	ΔG^θ (kJ/mol)	ΔH (kJ/mol)	ΔS (J/(mol·K))
303	215.14	−13.53		
318	242.90	−14.52	16.86	99.77
333	395.58	−16.56		

3.5. Selectivity and Cycling Stability

For practical testing, T-HMCO-4 was packed into a fixed-bed glass column, and real salt lake brine from Xinjiang was circulated through the bed with a peristaltic pump (20 mL/min) until saturation; the complete column protocol is given in Section 2.5. Under this operating mode, T-HMCO-4 reached 1.56 mg/g (Figure 10a), lower than in LiCl solution (4.42 mg/g).

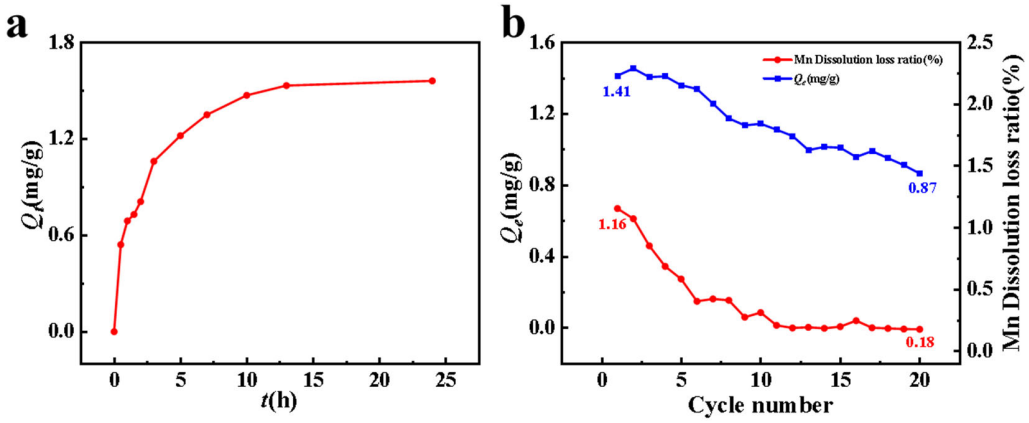


Figure 10. (**a**) Adsorption curve of T-HMCO-4 in salt lake brine; (**b**) Cycling performance of T-HMCO-4 over 20 cycles.

The gap between the brine capacity (1.56 mg/g) and the LiCl capacity (4.42 mg/g) is governed by four brine-specific factors. (1) pH: Li^+ uptake by manganese ion-sieves proceeds through H^+/Li^+ exchange, so pH exerts a first-order effect on the uptake. (2) Lower Li^+ concentration: the brine contains 125 mg/L Li^+, less than half of the 300 mg/L used in the LiCl tests, and the Langmuir fit (Table 5) predicts a lower equilibrium uptake at a lower concentration. (3) Competing ions and viscosity: the coexisting Na^+, K^+, and Mg^{2+} total ≈ 115 g/L; the resulting viscosity and competitive adsorption lower the Li^+ mobility, and the intra-particle diffusion analysis (Section 3.4) identified internal mass transfer as the rate-limiting step. (4) Operating mode: the brine test was run in a fixed bed at 20 mL/min, far from the 24 h equilibrium contact of the batch LiCl tests.

Li^+ uptake by manganese ion-sieves proceeds through H^+/Li^+ exchange. In the pH-dependence study on the Co-doped powder, the adsorption capacity increased from 25.41 mg/g at pH 6 to 39.28 mg/g at pH 12 (+54.6%), because a higher OH^- activity

consumes the H+ released by the exchange and drives the equilibrium toward Li+ uptake. The brine used here is acidic (pH 5.30), below the lowest pH examined, so a markedly suppressed uptake is expected; the 1.56 mg/g obtained in the brine is consistent with this trend. Raising the brine pH before adsorption would increase the uptake, but at high pH the Mn–OH complexation raises the Mn dissolution loss during cycling, which is why pH 10 was selected as the adsorption condition in this work and why pH pre-adjustment of the brine requires a cost–benefit evaluation (Section 4). The separation factor (α) was calculated from Equation (9). The values were 357.0 (Li^+/Na^+), 256.5 (Li^+/K^+), 225.4 (Li^+/Mg^{2+}), and 41.87 (Li^+/Ca^{2+}) (Table 7). The Li^+/Mg^{2+} factor fell from 676.50 (HMCO-4 powder, Table 1) to 225.4 (granulated T-HMCO-4), a 66.7% reduction. This drop is attributed to the polymer matrix partially blocking the spinel surface and reducing Li^+ access to the ion-sieve channels. By contrast, the Li^+/Ca^{2+} factor rose from 5.15 (powder) to 41.87 (granulated). This may reflect a polymer sieving effect, in which the St/DVB network preferentially excludes the larger hydrated Ca^{2+} ions from the particle interior and so raises the apparent Li^+/Ca^{2+} selectivity. Further studies are needed to confirm this.

Table 7. Adsorption selectivity of T-HMCO-4 in actual salt lake brine.

Ions	C_0 (mg/L)	C_e (mg/L)	K_i (L/g)	α (Li^+/M_i)
Li^+	125.1	76.07	1.96×10^{-2}	1
Na^+	27,740	27,690	5.49×10^{-5}	357.0
K^+	23,930	23,870	7.64×10^{-5}	256.5
Mg^{2+}	63,110	62,930	8.69×10^{-5}	225.4
Ca^{2+}	31.66	31.18	4.68×10^{-4}	41.87

The high flow rate was chosen to evaluate throughput, but the short contact time limited the capacity. Lower flow rates are expected to improve Li^+ uptake significantly, since the intra-particle diffusion analysis showed that internal mass transfer is the rate-limiting step.

Despite these changes, the granule keeps good selectivity, so the ion-sieve effect survives granulation. The trade-off between the lower Li^+/Mg^{2+} and higher Li^+/Ca^{2+} selectivity reflects the combined effect of the ion-sieve mechanism and the polymer matrix.

Table 8 summarizes the mass balance of the fixed-bed saturation run reported in Table 7. Of the 25.02 mg of Li^+ in the 200 mL feed, 15.21 mg remained in the brine after saturation and 9.81 mg (39.2% of the fed Li^+) was captured by the bed (bed charge ≈ 6.3 g), consistent with the reported capacity of 1.56 mg/g. The balances of the coexisting ions closed simultaneously: the removals of Na^+, K^+, and Mg^{2+} were only 0.18%, 0.25%, and 0.29%, respectively. On a molar basis, 1.41 mmol of Li^+ and 1.48 mmol of Mg^{2+} were captured from a feed with a Mg^{2+}/Li^+ molar ratio of ≈144, i.e., the bed enriched Li^+ over Mg^{2+} by roughly 137-fold. After saturation, the bed was eluted with 200 mL of 0.5 mol/L HCl. If elution is quantitative, the adsorbed Li^+ load corresponds to an eluate concentration of ≈49 mg/L; the capacity regeneration observed between the cycles of the cycling test (Figure 10b) indicates nearly complete desorption under this protocol. Because only 200 mL of brine was processed per bench-scale run, this eluate concentration reflects the small processed volume rather than a limit of the bed; in continuous operation, in which many bed volumes are loaded before elution, the eluate concentration rises accordingly. In either case, the decisive figure for downstream purification is the Li^+/Mg^{2+} mass ratio, which improves from ≈1:505 in the brine to ≈1:3.7 in the eluate.

Table 8. Mass balance of the fixed-bed saturation run of T-HMCO-4 in actual salt lake brine.

Ion	Feed (mg)	Remaining in Brine (mg)	Adsorbed (mg)	Removal (%)
Li^+	25.02	15.21	9.81	39.2
Na^+	5548	5538	10.0	0.18
K^+	4786	4774	12.0	0.25
Mg^{2+}	12,622	12,586	36.0	0.29
Ca^{2+}	6.33	6.24	0.10	1.5

After 20 adsorption–desorption cycles in the same brine, T-HMCO-4 kept 62% of its initial capacity (from 1.41 to 0.87 mg/g), and Mn dissolution fell from 1.16% in the first cycle to a stabilized 0.18% (Figure 10b). The capacity loss can be attributed to three mechanisms of different weights. (i) Irreversible consumption of the most reactive sites: Mn dissolution peaked in the first cycle (1.16%) and decayed to a stable 0.18%, indicating that near-surface Mn^{3+}-rich sites, which are the most vulnerable to disproportionation ($2Mn^{3+} \rightarrow Mn^{4+} + Mn^{2+}$), are consumed first; this removes a disproportionate share of the high-affinity sites. (ii) Incomplete regeneration per cycle: the eluent does not fully penetrate the mesopore network within the fixed contact time, so a small fraction of sites remains Li^+-occupied, consistent with the incomplete transformation discussed in Section 3.3. (iii) Progressive pore blockage: salts from the high-salinity brine ($Na^+ + K^+ + Mg^{2+} \approx 115$ g/L) can deposit inside the mesopores during the wash and elution stages and gradually mask adsorption sites. Importantly, both the capacity decay and the Mn dissolution stabilize after the first few cycles, and the post-cycling SEM-EDS (Figure 11) shows intact spheres with preserved mesopores and a uniformly distributed Co-doped active component; the granule therefore approaches a stable residual capacity rather than undergoing progressive structural collapse, which we attribute to the Co-doping suppression of the Jahn-Teller distortion.

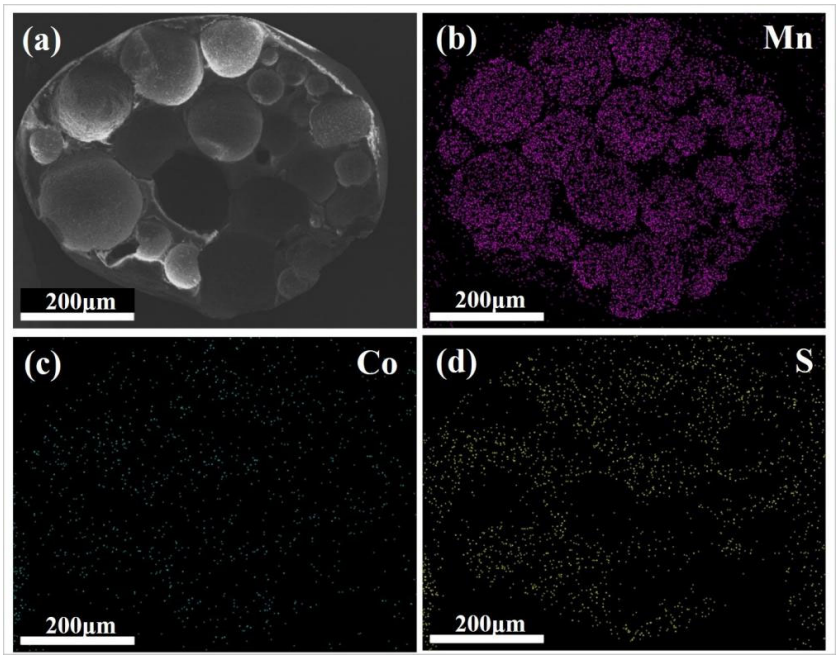


Figure 11. (**a**) T-HMCO-4 after 20 cycles and (**b**–**d**) EDS elemental mapping of T-HMCO-4.

4. Conclusions and Perspectives

This study reports a pore-engineering approach to the suspension granulation of manganese-based lithium ion-sieves, using solid paraffin as a mesoporous porogen to

solve the powder-forming problem that limits industrial use. Co doping suppressed the Jahn-Teller distortion by raising the Mn^{4+} fraction from 65.77% to 72.16%, and the optimized powder reached 33.36 mg/g in LiCl solution with 89.0% capacity retention after five cycles. For granulation, OTMS modification changed the powder surface from hydrophilic (contact angle 23.09°) to hydrophobic (149.62°), enabling uniform dispersion in the organic monomer phase. Among the three porogen conditions, solid paraffin gave the best result: T-HMCO-4 reached a BET area of 82.00 m^2/g, a large increase over the non-porogen control, with a mechanical strength of 6.39 N. It delivered 4.42 mg/g in LiCl solution and 1.56 mg/g in real salt lake brine, with high selectivity (α = 357.0, 256.5, 225.4, and 41.87 for Na^+, K^+, Mg^{2+}, and Ca^{2+}) and 62% capacity retention over 20 cycles, while Mn dissolution stabilized at 0.18%. The granulated capacity is lower than the powder capacity, but this loss is inherent to polymer-encapsulated systems and is offset by the practical benefits of granulation: better dispersibility, lower column pressure drop, and no adsorbent loss during continuous operation. Solid paraffin is an effective mesoporous porogen for LIS granulation, and the combined strategy offers a route from powder synthesis to practical adsorbent fabrication for lithium extraction from salt lake brines.

Several challenges still stand in the way of industrial use. The capacity in real brine (1.56 mg/g) is limited by the suboptimal brine pH, the incomplete acid transformation of the granule (14.83%), and the high polymer-to-adsorbent ratio (about 80 wt%). Future work should: improve acid penetration and site utilization through higher porogen-to-monomer ratios, smaller granule diameters, and more hydrophilic binder chemistry; reduce the polymer matrix ratio through crosslinker optimization and reinforcing fillers while keeping mechanical strength; evaluate pH pre-adjustment and its cost–benefit for large-scale brine processing; quantify the eluate composition and develop multi-stage elution and counter-current columns to improve cumulative Li^+ recovery; and test the solid paraffin porogen concept on other adsorbents, such as titanium-based lithium ion-sieves. Meeting these challenges should close the gap between laboratory demonstration and industrial lithium extraction from salt lake brine.

Author Contributions: Conceptualization, Q.L. and Z.H.; Methodology, Q.L. and Z.H.; Validation, M.L.; Formal analysis, Q.L.; Investigation, Q.L., Z.H. and M.L.; Resources, X.S.; Data curation, Q.L.; Writing—original draft, Q.L.; Writing—review & editing, Z.H., M.L. and X.S.; Visualization, Q.L.; Supervision, X.S.; Project administration, X.S. All authors have read and agreed to the published version of the manuscript.

Funding: This research received no external funding.

Data Availability Statement: Data is contained within the article.

Conflicts of Interest: The authors declare no conflicts of interest.

References

1. Harper, G.; Sommerville, R.; Kendrick, E.; Driscoll, L.; Slater, P.; Stolkin, R.; Walton, A.; Christensen, P.; Heidrich, O.; Lambert, S.; et al. Recycling lithium-ion batteries from electric vehicles. *Nature* **2019**, *575*, 75–86. [CrossRef]
2. Liu, J.; Bao, Z.; Cui, Y.; Dufek, E.J.; Goodenough, J.B.; Khalifah, P.; Li, Q.; Liaw, B.Y.; Liu, P.; Manthiram, A.; et al. Pathways for practical high-energy long-cycling lithium metal batteries. *Nat. Energy* **2019**, *4*, 180–186. [CrossRef]
3. Fan, E.; Li, L.; Wang, Z.; Lin, J.; Huang, Y.; Yao, Y.; Chen, R.; Wu, F. Sustainable recycling technology for Li-ion batteries and beyond: Challenges and future prospects. *Chem. Rev.* **2020**, *120*, 7020–7063. [CrossRef]
4. Wu, F.; Maier, J.; Yu, Y. Guidelines and trends for next-generation rechargeable lithium and lithium-ion batteries. *Chem. Soc. Rev.* **2020**, *49*, 1569–1614. [CrossRef]
5. Yang, S.; Wang, Y.; Pan, H.; He, P.; Zhou, H. Lithium extraction from low-quality brines. *Nature* **2024**, *635*, 110–119. [CrossRef]
6. Zhu, R.; Wang, S.; Srinivasakannan, C.; Li, S.; Yin, S.; Zhang, L.; Jiang, X.; Zhou, G.; Zhang, N. Lithium extraction from salt lake brines with high magnesium/lithium ratio: A review. *Environ. Chem. Lett.* **2023**, *21*, 1611–1626. [CrossRef]

7. Liu, Y.; Ma, B.; Lü, Y.; Wang, C.; Chen, Y. A review of lithium extraction from natural resources. *Int. J. Miner. Metall. Mater.* **2023**, *30*, 209–224. [CrossRef]
8. Li, Z.; Chen, I.-C.; Cao, L.; Liu, X.; Huang, K.-W.; Lai, Z. Lithium extraction from brine through a decoupled and membrane-free electrochemical cell design. *Science* **2024**, *385*, 1438–1444. [CrossRef]
9. Yang, F.; Lv, X.; Duan, L.; Wang, L. Isolated soy protein/TiO_2 membrane adsorber for selective separation of lithium ion. *SSRN Electron. J.* **2022**. [CrossRef]
10. Weng, D.; Duan, H.; Hou, Y.; Huo, J.; Chen, L.; Zhang, F.; Wang, J. Introduction of manganese based lithium-ion sieve-A review. *Prog. Nat. Sci. Mater. Int.* **2020**, *30*, 139–152. [CrossRef]
11. Deng, Y.; Chai, G.; Zhang, Y. Research progress on lithium extraction from salt-lake brine. *J. Ind. Eng. Chem.* **2025**, *148*, 92–108. [CrossRef]
12. Xiao, J.; Sun, S.; Wang, J.; Li, P.; Yu, J. Synthesis and adsorption properties of $Li_{1.6}Mn_{1.6}O_4$ spinel. *Ind. Eng. Chem. Res.* **2013**, *52*, 11967–11973. [CrossRef]
13. Bao, L.-R.; Zhang, J.-Z.; Tang, W.-P.; Sun, S.-Y. Synthesis and adsorption properties of metal oxide-coated lithium ion-sieve from salt lake brine. *Desalination* **2023**, *546*, 116196. [CrossRef]
14. Zhao, K.; Tong, B.; Yu, X.; Guo, Y.; Xie, Y.; Deng, T. Synthesis of porous fiber-supported lithium ion-sieve adsorbent for lithium recovery from geothermal water. *Chem. Eng. J.* **2022**, *430*, 131423. [CrossRef]
15. Gao, Y.; Sun, Y.; Chen, L.; Tan, Y.; Fan, R.; Hai, C.; Zhang, H. Progress of research in titanium-based lithium-ion sieves for the extraction of lithium from salt lake brine. *ACS Omega* **2025**, *10*, 11643–11657. [CrossRef]
16. Toprak, S.; Demir, M.M. One-step hydrothermal synthesis of spinel manganese oxide ion-sieve from commercial γ-MnO_2 and its uptake performance for lithium. *Chemosphere* **2024**, *369*, 143891. [CrossRef]
17. Jia, H.; Wang, P.; Jin, L.; Gu, S.; Yu, J. Electrochemical quartz crystal microbalance study of lithium-ion dynamics in $LiMn_2O_4$/λ-MnO_2 for ion-selective capacitive deionization. *Electrochim. Acta* **2024**, *513*, 145555. [CrossRef]
18. Vörös, M.; Garcia, J.C.; Warburton, R.E.; Iddir, H.; Greeley, J.; Curtiss, L.A. Jahn-Teller distortion and disproportionation in spinel lithium manganese oxides from first principles. *ECS Meet. Abstr.* **2018**, *MA2018-01*, 358. [CrossRef]
19. Zhao, Q.; Yao, T.; Liu, Y.; Zheng, X.; Yang, P. Multi-dimensional regulation of the cycling stability of lithium manganese oxides: A review. *Desalin. Water Treat.* **2025**, *325*, 101591. [CrossRef]
20. Li, X.; Sun, Y.; Zhou, L.; Wang, H.; Xie, B.; Lu, W.; Ning, J.; Hu, Y. Suppressing Jahn–Teller distortion and locking lattice water with doped Fe(III) in birnessite toward fast and stable zinc-ion batteries. *Mater. Horiz.* **2024**, *11*, 4133–4143. [CrossRef]
21. Chen, L.; Tan, B.; Fang, Y.; Hu, L.; Zhou, J.; Liang, Y.; Pan, J.; Zhou, J. Manganese-based lithium-ion sieve prepared by chelation with aluminum sec-butoxide for an extremely low manganese dissolution rate and extended service life. *Chem. Eng. J.* **2025**, *511*, 162274. [CrossRef]
22. Chen, Z.; Liu, P.; Cao, Y.-L.; Xie, Y.-L. Co ion-modified Li1.6Mn1.6O4 with enhanced Li+ adsorption performance and cyclic stability. *J. Mater. Sci.* **2025**, *60*, 15140–15155. [CrossRef]
23. Zhang, G.; Hai, C.; Zhou, Y.; Zhang, J.; Liu, Y.; Zeng, J.; Shen, Y.; Li, X.; Sun, Y.; Wu, Z.; et al. Synthesis and performance estimation of a granulated PVC/PAN-lithium ion-sieve for Li+ recovery from brine. *Sep. Purif. Technol.* **2023**, *305*, 122431. [CrossRef]
24. Tian, L.; Yang, Y.; Chen, G.; Tiraferri, A.; Liu, B. Efficient lithium extraction from shale gas wastewater using sodium alginate/H1.33Mn1.67O4 composite granular adsorbents. *ACS EST Eng.* **2023**, *3*, 1676–1685. [CrossRef]
25. Liu, P.; Yan, X.; Chen, Z.; Qin, Y.; Yang, L.; Ma, J. Preparation of half-coated manganese oxide lithium ion-sieve precursor with low manganese dissolution loss for lithium recovery. *J. Water Process Eng.* **2025**, *74*, 107785. [CrossRef]
26. Zhao, Q.; Yao, T.; Liu, Y.; Zheng, X.; Yang, P. Lithium extraction from oil and gas produced water with spherical manganese-based lithium ion sieve: Preparation, adsorption mechanism, and fixed-bed application. *Desalin. Water Treat.* **2026**, *325*, 101686. [CrossRef]
27. Deng, G.; Jiang, R.; Hou, Z.; Feng, Y. Fabrication and adsorption behavior of a lithium manganese oxide-based β-Cyclodextrin/PVDF composite membrane for lithium extraction from salt lake brine. *J. Environ. Chem. Eng.* **2026**, *14*, 122349. [CrossRef]
28. Feng, Y.; Zhang, Y.; Wang, L.; Wang, S.; Xu, L.; Han, S.; Deng, T. A hollow hemispherical mixed matrix lithium adsorbent with high interfacial interaction for lithium recovery from brine. *Separations* **2024**, *11*, 301. [CrossRef]
29. Li, X.; Li, X.; Zheng, M.; Shi, J.; Yang, L.; Yang, Y.; Chen, G.; Bai, S.; Lin, X.; Liu, W.; et al. A novel blended adsorbent granule of crown ether polymer mixed with Mn-based lithium-ion sieves for efficient lithium recycling from shale gas wastewater. *Desalination* **2026**, *619*, 119576. [CrossRef]
30. Wang, L.; Wang, L.; Xue, S.; He, L.; Wang, X.; Lv, Y. Preparation of granular lithium ion sieve with high adsorption capacity and stable performance for lithium recovery. *J. Water Process Eng.* **2025**, *77*, 108600. [CrossRef]
31. Du, J.; Ma, J.; Cui, X.; Liu, X.; Wang, D.; Wang, B.; Zhang, X.; Zhai, R.; Zhu, J.; Zuo, H.; et al. Synthesis and adsorption performance of modified granular lithium ion sieve. *JOM* **2026**, *78*, 2622–2632. [CrossRef]

32. Chaudhary, V.; Sharma, S. Suspension polymerization technique: Parameters affecting polymer properties and application in oxidation reactions. *J. Polym. Res.* **2019**, *26*, 102. [CrossRef]
33. Udoetok, I.A.; Karoyo, A.H.; Ubuo, E.E.; Asuquo, E.D. Granulation of lithium-ion sieves using biopolymers: A review. *Polymers* **2024**, *16*, 1520. [CrossRef]
34. Peterson, C.H.; Werber, J.R.; Lee, H.K.; Hillmyer, M.A. Tailored mesoporous microspheres by polymerization-induced microphase separation in suspension. *ACS Appl. Polym. Mater.* **2022**, *4*, 4219–4233. [CrossRef]
35. Duan, L.; Fan, J.; Chen, G.; Qiu, P.; Zhang, X.; Zhai, X. Synthesis of porous PEGDMA microspheres via suspension polymerization and the effect of different porogens on the porous structure. *Colloids Surf. A* **2025**, *709*, 136125. [CrossRef]
36. Mohamed, M.H.; Wilson, L.D. Porous copolymer resins: Tuning pore structure and surface area with non reactive porogens. *Nanomaterials* **2012**, *2*, 163–186. [CrossRef]
37. Hong, H.-J.; Park, I.-S.; Ryu, T.; Kim, B.-G.; Chung, K.-S. Macroporous hydrogen manganese oxide/Al2O3 for effective lithium recovery from seawater: Effects of the macropores vs mesopores. *Ind. Eng. Chem. Res.* **2019**, *58*, 8342–8348. [CrossRef]
38. Koilraj, P.; Smith, S.M.; Yu, Q.; Ulrich, S.; Sasaki, K. Encapsulation of a powdery spinel-type Li+ ion sieve derived from biogenic manganese oxide in alginate beads. *Powder Technol.* **2016**, *301*, 1201–1207. [CrossRef]
39. Fonseka, C.; Ryu, S.; Naidu, G.; Kandasamy, J.; Thiruvenkatachari, R.; Vigneswaran, S. Europium adsorption by granulated Cr-MIL-PMIDA metal-organic frameworks and dynamic fixed bed column modelling. *J. Water Process Eng.* **2023**, *56*, 104475. [CrossRef]
40. Ho, Y.S.; McKay, G. Pseudo-second order model for sorption processes. *Process Biochem.* **1999**, *34*, 451–465. [CrossRef]
41. Wang, J.; Guo, X. Adsorption kinetic models: Physical meanings, applications, and solving methods. *J. Hazard. Mater.* **2020**, *390*, 122156. [CrossRef]
42. Langmuir, I. The adsorption of gases on plane surfaces of glass, mica and platinum. *J. Am. Chem. Soc.* **1918**, *40*, 1361–1403. [CrossRef]
43. Al-Ghouti, M.A.; Da'ana, D.A. Guidelines for the use and interpretation of adsorption isotherm models: A review. *J. Hazard. Mater.* **2020**, *393*, 122383. [CrossRef]
44. Capsoni, D.; Bini, M.; Chiodelli, G.; Massarotti, V.; Azzoni, C.B.; Mozzati, M.C.; Comin, A. Inhibition of Jahn-Teller cooperative distortion in LiMn2O4 spinel by transition metal ion doping. *Phys. Chem. Chem. Phys.* **2001**, *3*, 2162–2166. [CrossRef]
45. Shivakumar, K.R.; Zolfaghari, A.; Safari, S.; Wu, F.; Bishop, B.A.; Chen, N.; Robbins, L.J.; Alessi, D.S. Lithium extraction using zirconium oxide coated lithium manganese oxide ion-exchange adsorbents. *Chem. Commun.* **2025**, *61*, 11013–11016. [CrossRef]
46. Wu, X.; Zhang, H.; Zhang, X.; Guan, Q.; Tang, X.; Wu, H.; Feng, M.; Wang, H.; Ou, R. Sustainable lithium extraction enabled by responsive metal-organic frameworks with ion-sieving adsorption effects. *Proc. Natl. Acad. Sci. USA* **2024**, *121*, e2309852121. [CrossRef]
47. Zhizhchenko, A.Y.; Shabalina, A.V.; Aljulaih, A.A.; Gurbatov, S.O.; Kuchmizhak, A.A.; Iwamori, S.; Kulinich, S.A. Stability of octadecyltrimethoxysilane-based coatings on aluminum alloy surface. *Materials* **2022**, *15*, 1804. [CrossRef]
48. Ebelegi, A.N.; Ayawei, N.; Wankasi, D. Interpretation of adsorption thermodynamics and kinetics. *Open J. Phys. Chem.* **2020**, *10*, 166–182. [CrossRef]

Disclaimer/Publisher's Note: The statements, opinions and data contained in all publications are solely those of the individual author(s) and contributor(s) and not of MDPI and/or the editor(s). MDPI and/or the editor(s) disclaim responsibility for any injury to people or property resulting from any ideas, methods, instructions or products referred to in the content.